https://doi.org/10.5194/gmd-2020-184
Preprint. Discussion started: 21 September 2020

Geoscientific Model Development Discussions

A discontinuous Galerkin finite element model for fast channelized lava flows v1.0

Colton J. Conroy[1,2] and Einat Lev[1]

Lamont-Doherty Earth Observatory[1]
Columbia University in the City of New York, USA

Roy M. Huffington Department of Earth Sciences[2]
Southern Methodist University, Dallas, TX, USA

Abstract

Lava flows present a significant natural hazard to communities around volcanoes and are typically slow moving ($<$ 1 to 5 cm/s) and laminar. Recent lava flows during the 2018 eruption of Kilauea Volcano, Hawai'i, however, reached speeds as high as 11 m/s and were transitional to turbulent. The Kilauea flows formed a complex network of braided channels departing from the classic rectangular channel geometry often employed by lava flow models. To investigate these extreme dynamics we develop a new lava flow model that incorporates nonlinear advection as well as a nonlinear expression for the fluid viscosity. The model makes use of novel discontinuous Galerkin (DG) finite element methods and resolves complex channel geometry through the use of unstructured triangular meshes. We verify the model against an analytic test case and demonstrate convergence rates of $p + 1/2$ for polynomials of degree p. Direct observations recorded by Unoccupied Aerial Systems (UASs) during the Kilauea eruption provide inlet conditions, constrain input parameters, and serve as a benchmark for model evaluation.

1 Introduction

On May 3, 2018, Kilauea Volcano on the Island of Hawai'i began to erupt from new fissures in the lower East Rift Zone at the center of the Leilani Estates Subdivision. Before ceasing in early August 2018, the lava flows destroyed over 650 structures and caused significant damage to infrastructure and essential facilities. During the second half of the eruption the flow field established a complex braided channel system (which is common to many basaltic flows), originating from Fissure number 8 (see Figure 1). The "Fissure 8" flows were unique in the fact that they produced channelized flows reaching speeds as high as 11 m/s (Neal et al., 2019). These high speeds, coupled with channel geometry (e.g. constrictions) produced Reynolds numbers ($Re > 3000$) that were significantly higher than typical lava flows. At these conditions sections of the lava flow field were in the transitional to turbulent regime implying that inertial forces did not necessarily dominate viscous forces. Any attempt to model the fluid resistance, therefore, needs to account for basal friction as well as the viscous forces normally considered by lava flow models.

https://doi.org/10.5194/gmd-2020-184
Preprint. Discussion started: 21 September 2020

Geoscientific Model Development Discussions
Open Access
EGU

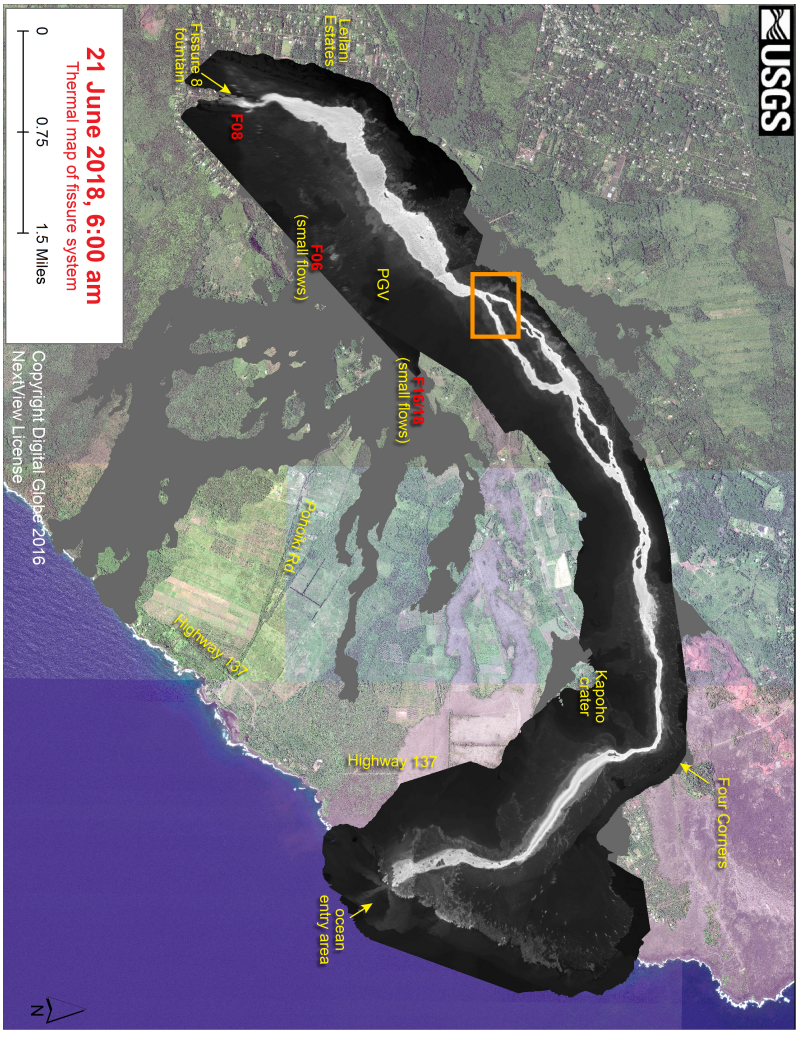

Figure 1: A satellite image (colored, in the background, by DigitalGlobe) overlayed by a thermal aerial orthomosaic (grayscale) where the white and light gray areas reveal the path of the Fissure 8 flow channel as it was on June 21st, 2018. Data and map by USGS. The orange rectangle depicts the area of UAS site 8, from where the video we analyzed was captured on June 22nd, 2018. The flat gray areas south of the active flow channel demarcate the areas inundated by lava during the early stages of the eruption. North is up. PGV is the Puna Geothermal Ventures power plant that was heavily impacted by the lava.

https://doi.org/10.5194/gmd-2020-184
Preprint. Discussion started: 21 September 2020

Geoscientific Model Development Discussions
Open Access
EGU

Typical "operational" lava flow models simulate unconfined lava flow in a 2D plan view [e.g., SCIARA (Crisci et al., 2004-04), MAGFLOW (Vicari et al., 2007), LavaPL (Connor et al., 2012), VOLCFLOW (Kelfoun and Vargas, 2015)] using either cellular automata or depth-averaged equations in an effort to forecast the area of land inundated by the lava. It is often difficult, however, for these models to accurately reproduce the complicated braided channel network such as those created by "Fissure 8." These braided channel networks are common in natural flows (e.g., Dietterich and Cashman, 2014-08) and understanding the evolution of the velocity, rheology, and temperature fields (e.g. in response to pulsating effusion) within these channels is critical to hazard mitigation (Patrick et al., 2019). Direct measurements of lava properties in situ is usually extremely difficult and dangerous. Modeling lava dynamics within the bounds of an established channel can help to better understand material properties of the flowing lava and inform models and decisions.

Previous attempts to model channelized lava flows have made use of simple heuristic formulas such as Jeffreys equation for laminar flows (Harris and Rowland, 2015) or Chezy approximations for higher speed flows (Baloga et al., 1995). While convenient, the use of these equations has largely been dictated by the fact that it has been difficult to obtain the physical data necessary for advanced modeling efforts (e.g. channel domain boundaries, inlet boundary conditions, topography, etc). However, with the advent of Unoccupied Aerial Systems (UASs, or 'drones') and their ability to survey active lava fields, we now have access to the data required by sophisticated numerical methods.

Commensurate with this development in observational capabilities, we introduce a numerical method for modeling fast moving lava flows in complex channels. The large Reynolds number associated with these lava flows means that the dynamics can be well approximated by two-dimensional depth-integrated equations for mass, momentum, and energy. We build approximate solutions to these equations using discontinuous Galerkin (DG) finite element methods (Cockburn and Shu, 2001) and discretize the complexities of the lava channel domain with unstructured triangular meshes. The DG method, in particular, seems to be a judicious choice for modeling lava flows because of the weak constraints it places on the continuity of the lava flow field. This allows the discontinuous thermodynamic properties of the lava to be readily captured by the model. Further, even though the DG method is discontinuous it still conserves mass, momentum, and energy both locally and globally (Cockburn and Shu, 2001).

A major component of our investigation involves quantifying the bottom stress that resists the flow of the lava. Typical friction drag laws do not take into account the viscosity of the fluid (due to the assumption that the fluids inertial acceleration is much greater than its internal resistance), however, in our particular case the flow is not fully turbulent; internal resistance needs to be taken into account in some fashion. To account for this effect we introduce a stress term at the bottom boundary of the lava field that is a function of the temperature and vorticity of the flow field. We solve a thermal boundary layer problem to calculate the non-linear viscosity at the bottom boundary and utilize the vorticity to determine a virtual length scale over which the interior velocity goes from the depth-averaged value to a value of zero. This results in a bottom stress approximation that does not make use of a friction factor (e.g. Manning's n). This allows scientists to study physical properties of the lava that cannot be measured directly, for example, the lava thickness and viscosity.

Model verification consists of solving an analytic test case using forcing functions that

https://doi.org/10.5194/gmd-2020-184
Preprint. Discussion started: 21 September 2020

Geoscientific Model Development Discussions
Open Access
EGU

we choose to exactly satisfy the equations of motion. The dynamical equations are coupled to the energy equation through a non-linear stress-strain relationship and results indicate that for smooth solutions the method converges to the exact solution at a rate of $p+1/2$ for polynomials of degree p.

The remainder of this paper is organized as follows: in §2 we present the math model along with the bottom stress calculation and detail its nuances. We present the DG numerical discretization of the math model in §3 and verify the model in §4. In §5 we evaluate the model against observations of lava flows from the 2018 eruption of Kilauea volcano. We present misfit errors and root mean square (rms) errors for the velocity field from a braided channel section of Fissure 8, and provide quantitative insight into physical quantities of the lava flow field in this area including its thickness and viscosity. We close the paper in §6 with some discussion and conclusions.

2 Mathematical model

The mathematical model consists of depth-integrated equations of mass, momentum, and energy in Cartesian–coordinates (x, y) (see Figure 2 for a diagram) over a time-dependent domain $\Omega(t) \subset \mathbb{R}^2$ written in conservative form (see Kubatko et al. (2006)),

$$\begin{aligned}
\frac{\partial \zeta}{\partial t} + \frac{\partial Hu}{\partial x} + \frac{\partial Hv}{\partial y} &= 0, \\
\frac{\partial Hu}{\partial t} + \frac{\partial}{\partial x}\left(Hu^2 + p\right) + \frac{\partial Huv}{\partial y} + gH\beta_x &= g\zeta\frac{\partial h}{\partial x} - \tau^{(x)}Hu, \\
\frac{\partial Hv}{\partial t} + \frac{\partial Huv}{\partial x} + \frac{\partial}{\partial y}\left(Hv^2 + p\right) + gH\beta_y &= g\zeta\frac{\partial h}{\partial y} - \tau^{(y)}Hv, \\
\frac{\partial HT}{\partial t} + \frac{\partial HuT}{\partial x} + \frac{\partial HvT}{\partial y} &= Q_{surf} + Q_{base},
\end{aligned} \tag{1}$$

where $H = h + \zeta$ is the total depth of flow of the lava, h is the steady depth of flow, and ζ is the free surface elevation, see Figure 2 for the details. The depth-averaged horizontal velocity vector, $\mathbf{u} = (u,\ v)$, is defined as $u = \frac{1}{H}\int_{-h}^{\zeta} \tilde{u}\ \mathrm{d}z$ and $v = \frac{1}{H}\int_{-h}^{\zeta} \tilde{v}\ \mathrm{d}z$; g is acceleration due to gravity, $p = \frac{1}{2}g\left(H^2 - h^2\right)\cos\theta$ is the dynamic pressure, θ is the bottom slope, β_x and β_y are the $x-$ and $y-$components of the slope, $\partial h/\partial x$ and $\partial h/\partial y$ quantify the gradient in the steady depth of flow, $T = \frac{1}{H}\int_{-h}^{\zeta} \tilde{T}\ \mathrm{d}z$ is the depth-averaged temperature in degrees Kelvin, and Q_{surf} and Q_{base} quantify heat transfer at the surface and the base/walls of the channel, respectively. We write the bottom stress term, $\mu(\partial\mathbf{u}/\partial z)|_{z=-h}$, which resists the flow of the lava, as $\tau^{(x,y)}H\mathbf{u}$, which gives the mathematical model the flexibility to use different stress approximations. For instance, if one sets $\tau^{(x,y)} =$ constant, then the bottom stress is linearly proportional to the mass flux. Many depth-integrated models utilize a Manning's n stress approximation that defines $\tau^{(x,y)}$ as a function of the velocity, flow depth, and an adjustable friction coefficient. We utilize an approximation due to Herschel and Bulkley (1926) that

https://doi.org/10.5194/gmd-2020-184
Preprint. Discussion started: 21 September 2020

Geoscientific Model Development Discussions
Open Access
EGU

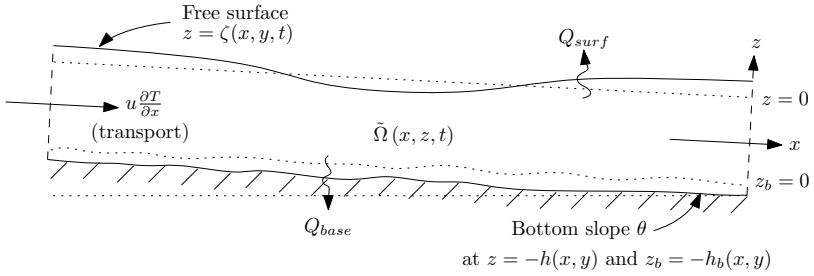

Figure 2: A vertical cross-section along the center line of the flow, showing the coordinates (x and z, with y the across-flow direction) and the heat transfer mechanisms considered in the model (conduction to the base, advection by the flow, and heat loss by radiation/convection at the surface).

quantifies the fluid stress in terms of a temperature dependent non-linear viscosity, see §2.1 for details.

The system of equations given by (1) are subject to the following dynamic and thermal boundary conditions:

- Channel wall boundary condition: no normal flow and heat loss due to conduction,

$$\mathbf{u}(x, y) \cdot \mathbf{n} \;=\; 0 \quad \text{and} \quad \rho c_p \frac{\partial T}{\partial x} \;=\; c_b \left(T - T_{wall}\right),$$

- Inlet boundary condition: prescribed velocity and heat content,

$$\mathbf{u}(x, y) \cdot \mathbf{n} \;=\; \text{prescribed} \quad \text{and} \quad \rho c_p T \;=\; \text{prescribed},$$

- Outlet boundary condition: zero change in normal velocity and heat content,

$$\frac{\partial \mathbf{u}}{\partial \mathbf{n}} \;=\; 0 \quad \text{and} \quad \rho c_p \frac{\partial T}{\partial \mathbf{n}} \;=\; 0,$$

where c_b is a conduction constant, T_{wall} is the channel wall temperature, ρ is the density of the lava, and c_p is the specific heat of the lava. It can be noted that the depth-integrated mass and momentum equations given in (1) are well studied in the literature and are commonly used to model shallow mass flows such as coastal ocean circulation and hurricane storm surge, see for example Dawson et al. (2011) and Kubatko et al. (2006). The addition of the energy equation complicates the solution of (1) due to the fact that the stress term $\tau^{(x,y)}$ is now a function of both non-linear velocity gradients and temperature.

2.1 The stress term

In the equations of motion we define the stress term using a Herchel-Bulkley model (Herschel and Bulkley, 1926),

$$\tau_{z\mathbf{x}} \;=\; \tilde{\mu} \frac{\partial \mathbf{u}}{\partial z} \;+\; \tau_{\text{yield}} \left[\text{sgn}\left(\frac{\partial \mathbf{u}}{\partial z}\right)\right], \tag{2}$$

https://doi.org/10.5194/gmd-2020-184
Preprint. Discussion started: 21 September 2020

Geoscientific Model Development Discussions
Open Access
EGU

where τ_{yield} is the yield strength of the fluid, sgn denotes the sign of the argument and $\tilde{\mu}$ is the non-linear viscosity defined as,

$$\tilde{\mu} \;=\; \mathcal{K}\left|\frac{\partial \mathbf{u}}{\partial z}\right|^{n-1}. \tag{3}$$

The symbol $\mathcal{K}$ in equation (3) represents the consistency of the lava and can be modeled solely as a function of temperature or as a function of its particle/bubble content (which in turn are functions of temperature), see Castruccio et al. (2010) and Castruccio et al. (2014) for example. A value of $n = 1$ corresponds to a Newtonian fluid while $n < 1$ or $n > 1$ corresponds to a non-Newtonian fluid. If $n > 1$ then the fluid viscosity increases with shear rate increases (known as shear thickening) while if $n < 1$ the fluid viscosity decreases as the shear rate increases (known as shear thinning). Typically, if the lava is sufficiently hot and degassed, then the lava stress can be modelled with a Newtonian approximation and $n = 1$. However, if bubbles and/or crystals are present in the lava (depending on the lava source and the amount of degassing that has occurred) then these structures will deform and realign under an applied shear stress which consequently causes the effective viscosity of the lava to become thinner in some situations and thicker in others (depending on how the structures rearrange).

2.1.1 Fluid consistency

We quantify the temperature dependency of the lava consistency ($\mathcal{K}$) using the VFT silicate melt model following Giordano et al. (2008),

$$\log \mathcal{K} \;=\; A + \frac{B}{T(\mathrm{K}) - C}, \tag{4}$$

where A is the value of $\log \mathcal{K}$ (Pa·s) at infinite temperature and B and C are parameters that depend on the composition of the lava. The model assumes that A is a constant for all silicate melts regardless of composition, and thus, it represents the high temperature limit for silicate melt viscosity. Once the parameter A is fixed then the parameters B and C are determined via a linear ensemble of combinations of oxide components and a subordinate number of multiplicative oxide cross terms, see Giordano et al. (2008) for the full details of the model.

2.1.2 The bottom stress

Once n and $\mathcal{K}$ have been defined in equation (3) we can write an expression for the vertical shear force acting over the thickness of the lava,

$$\frac{\partial \tau_{z\mathbf{x}}}{\partial z} \;=\; \frac{\partial}{\partial z}\left\{\tilde{\mu}\frac{\partial \mathbf{u}}{\partial z} \;+\; \tau_{\text{yield}}\left[\text{sgn}\left(\frac{\partial \mathbf{u}}{\partial z}\right)\right]\right\}. \tag{5}$$

We incorporate this expression into the depth-integrated equations of motion by integrating over the lava thickness,

$$\int_{-h}^{\zeta} \frac{\partial}{\partial z}\left\{\tilde{\mu}\frac{\partial \mathbf{u}}{\partial z} \;+\; \tau_{\text{yield}}\left[\text{sgn}\left(\frac{\partial \mathbf{u}}{\partial z}\right)\right]\right\} dz \;=\; 0 - \left\{\tilde{\mu}\frac{\partial \mathbf{u}}{\partial z} \;+\; \tau_{\text{yield}}\left[\text{sgn}\left(\frac{\partial \mathbf{u}}{\partial z}\right)\right]\right\}\Bigg|_{z=-h}, \tag{6}$$

https://doi.org/10.5194/gmd-2020-184
Preprint. Discussion started: 21 September 2020

Geoscientific Model Development Discussions
Open Access
EGU

where we have assumed that the vertical shear at the surface of the lava flow field is zero. Finally, we obtain an expression for $\boldsymbol{\tau}$ in the equations of motion by dividing (6) by the mass flux,

$$\boldsymbol{\tau} = -\frac{1}{\mathbf{u}H}\left\{\tilde{\mu}\frac{\partial \mathbf{u}}{\partial z} + \tau_{\text{yield}}\left[\text{sgn}\left(\frac{\partial \mathbf{u}}{\partial z}\right)\right]\right\}\Bigg|_{z=-h} = -\frac{1}{\mathbf{u}H}\left\{\tilde{\mu}\frac{\mathbf{u}}{\delta_z} + \tau_{\text{yield}}\left[\text{sgn}\left(\frac{\mathbf{u}}{\delta_z}\right)\right]\right\}\Bigg|_{z=-h}. \tag{7}$$

It can be noted that in the expression above, δ_z, is a measure of a virtual length over which the shear stress is applied. We determine δ_z by taking into account the vorticity of the lava flow field. More specifically, we define the vorticity as,

$$\boldsymbol{\omega} = \left(\frac{\partial w}{\partial y} - \frac{\partial v}{\partial z}\right)\hat{i} + \left(\frac{\partial w}{\partial x} - \frac{\partial u}{\partial z}\right)\hat{j} + \left(\frac{\partial u}{\partial y} - \frac{\partial v}{\partial x}\right)\hat{k}, \tag{8}$$

where $\hat{i}$, $\hat{j}$, and $\hat{k}$ are unit vectors in the $x-$, $y-$, and $z-$directions, respectively, and w is a measure of the vertical velocity. Depth-integrated models are inherently limited by the fact that they typically eliminate the vertical velocity in the equations of motion via scaling arguments and our model is no different. However, we circumvent this issue by making use of the kinematic boundary condition,

$$\frac{\partial \zeta}{\partial t} + u\frac{\partial \zeta}{\partial x}\Bigg|_{z=\zeta} + v\frac{\partial \zeta}{\partial y}\Bigg|_{z=\zeta} = w\Big|_{z=\zeta}, \tag{9}$$

coupled with the depth-integrated continuity equation (1) to obtain a measure of the vertical velocity w. More specifically, expanding derivatives in (1), solving for $\partial\zeta/\partial t$ while substituting this result into (9) and assuming that $(u, v, w) \approx (u(\zeta), v(\zeta), w(\zeta))$ yields,

$$w = \zeta\frac{\partial u}{\partial x} + \zeta\frac{\partial v}{\partial y}. \tag{10}$$

The relevant voriticty terms in (8) include the $\hat{i}$ and $\hat{j}$ components. By definition, $\partial u/\partial z = \partial v/\partial z = 0$ over the bulk of the lava thickness so that the vorticity component about the $x-$axis is $\partial w/\partial y$ and the vorticity component about the $y-$axis is $\partial w/\partial x$. Because the bottom boundary condition is modelled as a rigid wall where $\mathbf{u} = 0$ and the fluid is incompressible, a vorticity layer forms in the lava field near the solid boundary that resists the local rotation of the fluid (this is the reason why the rigid boundary does not deform). The vorticity created at the boundary resists the rotation of the interior and is equal to $\partial v/\partial z$ about the $x-$axis and $\partial u/\partial z$ about the $y-$axis (see Schlichting et al. (1968)). Now, if we assume that each vorticity component over the bulk of the flow is equal to each vorticity component in boundary layer at the coordinate point where $\partial u/\partial z = \partial v/\partial z$ is no longer equal to zero, then the virtual length over which the shear stress is applied is given by,

$$\delta_{z_x} = \frac{u}{\partial w/\partial x} \quad \text{and} \quad \delta_{z_y} = \frac{v}{\partial w/\partial y}. \tag{11}$$

It can be noted that as $(\partial w/\partial x, \partial w/\partial y)$ goes to 0, the vertical stress in the fluid goes to 0.

https://doi.org/10.5194/gmd-2020-184
Preprint. Discussion started: 21 September 2020

Geoscientific Model Development Discussions
Open Access
EGU

2.2 Heat transfer

As soon as lava effuses from an active vent it begins to degas and transfer heat to its surroundings. Lava cools through the mechanisms of radiation, conduction and convection. We quantify heat loss due to radiation via Stefan's law (Griffiths, 2000),

$$Q_{surf} \;=\; \frac{\epsilon\sigma_B}{\rho c_p H}\left(T^4 - T_{\text{atm}}^4\right), \tag{12}$$

where ϵ is the emissivity of the lava, σ_B is the Stefan-Boltzmann constant, and T_{atm} is the temperature of the surrounding atmosphere in degree Kelvin. When lava temperatures fall below the solidus (e.g., $\sim 950\ C$ for Kilauea lavas), buoyancy driven convection in the air above the lava becomes the dominant mode of heat transfer at the lava surface instead of radiation (due to crust formation) (Griffiths, 2000). In this case we set Q_{surf} in the energy equation to,

$$Q_{surf} \;=\; \frac{k_c}{H}\left(T - T_{\text{atm}}\right)^{4/3}, \tag{13}$$

where k_c is a heat transfer coefficient (e.g., Patrick et al., 2004) for more details. In addition to heat transfer at the free surface, lava loses heat to the ground and any walls it may be in contact with via conduction. In symbols we have (Patrick et al., 2004),

$$Q_{base} \;=\; \frac{k_T}{H}\left(T - T_{wall}\right), \tag{14}$$

where $T_{wall} = f(\mathbf{x})$ is the wall (or ground) temperature in contact with the lava flow field and k_T measures the thermal conductivity of the ground. We utilize equation (14) to determine the temperature near the bottom boundary of lava flow field which we use to evaluate the nonlinear viscosity in the bottom stress term in the equations of motion. More specifically, we can re-write (14) in terms of a depth-dependent thermal boundary-layer temperature, $\tilde{T}(z_b)$,

$$\frac{\partial \tilde{T}}{\partial z_b} \;=\; \frac{\tilde{k}_T}{h_b}\left(\tilde{T} - T_{\text{wall}}\right), \tag{15}$$

where z_b is the z-coordinate in the boundary layer, $\tilde{k}_T$ is the thermal boundary layer conductivity constant and $h_b(x, y)$ is the thickness of the thermal boundary layer (see Figure 2). Equation (15) is a non-homogeneous, constant coefficient ordinary differential equation that has the solution,

$$\tilde{T}(z_b) \;=\; (T_{\text{int}} - T_{\text{wall}})\exp\left(\frac{\tilde{k}_T}{h_b} z_b\right) \;+\; T_{\text{wall}}, \tag{16}$$

which gives an expression for the temperature profile over the thermal boundary layer of the lava ($z_b \in [0, -h_b]$). Evaluating equation (16) at $z_b = -h_b$ and setting the interior temperature (T_{int}) to the depth-integrated value (T), we have,

$$\tilde{T}\Big|_{z_b=-h_b} \;=\; (T - T_{\text{wall}})\exp\left(-\tilde{k}_T\right) \;+\; T_{\text{wall}}. \tag{17}$$

https://doi.org/10.5194/gmd-2020-184
Preprint. Discussion started: 21 September 2020

Geoscientific Model Development Discussions
Open Access
EGU

We use this temperature to evaluate the viscosity in the bottom stress approximation,

$$\tilde{\mu}(z=-h)=\tilde{\mu}\left(\tilde{T}(z_b=-h_b)\right). \tag{18}$$

The greater the thermal conductivity of the lava, the closer the boundary temperature is to the wall temperature, however, in general, there is usually a steep gradient in the temperature at the interface between the boundary of the flowing lava and the ground/walls that the lava is conducting heat to.

2.3 Steady depth of flow h

We have two options to calculate the steady depth of flow (h) of the lava. Our particular choice depends on the inflow data available to the model. For instance, if a full set of temporally varying inflow data is available, we set h equal to the time average thickness associated with the data, i.e.,

$$h=\frac{1}{(t_f-t_i)}\int_{t_i}^{t_f}\frac{\mathbf{q}_{\text{in}}\cdot\mathbf{n}}{w_{\text{in}}\,(\mathbf{u}_{\text{in}}\cdot\mathbf{n})}\,\mathrm{d}t, \tag{19}$$

where $\mathbf{q}_{\text{in}}\cdot\mathbf{n}$ is the inflow flux normal to the boundary and w_{in} is the width of the inflow boundary normal to the flow. If, however, the only inflow data available to the model is a set of time-averaged data, then we set h to the solution of the steady, linear system of equations associated with (20).

3 Numerical discretization

To develop our numerical methods, we rewrite the system of equations (1) in the compact form,

$$\frac{\partial U^{(i)}}{\partial t}\;+\;\nabla\cdot\mathbf{F}^{(i)}(\mathbf{U})\;=\;S^{(i)}(\mathbf{U}),\quad i=1,\;2,\;3,\;4 \tag{20}$$

where $U^{(i)}$, $\mathbf{F}^{(i)}$, and $S^{(i)}$ are the i-th row entries of the vectors $\mathbf{U}$, $\mathbf{S}$, and the flux function matrix $\mathbf{F}$, defined as,

$$\mathbf{U}=\begin{bmatrix}H\\ Hu\\ Hv\\ HT\end{bmatrix},\;\mathbf{F}=\begin{bmatrix}Hu, & Hv\\ Hu^2+p, & Huv\\ Huv, & Hv^2+p\\ HuT, & HvT\end{bmatrix},\;\mathbf{S}=\begin{bmatrix}0\\ -gH\beta_x+g\zeta\frac{\partial h}{\partial x}-\tau uH\\ -gH\beta_y+g\zeta\dfrac{\partial h}{\partial y}-\tau vH\\ Q_R+Q_c\end{bmatrix},$$

and $p=\frac{1}{2}g\,(H^2-h^2)\cos\theta$.

https://doi.org/10.5194/gmd-2020-184
Preprint. Discussion started: 21 September 2020

Geoscientific Model Development Discussions

3.1 Finite element partition

To apply a DG spatial discretization to our mathematical model (20) over a lava flow channel (see Figure 4 for example), we begin by introducing a partition of the two-dimensional
211 domain Ω. The complexities of the domain boundary, $\partial\Omega$, are such that an unstructured finite element partition (or mesh) is necessary to properly capture its intricacies. More specifically, we obtain unstructured triangulations (that we denote by $\mathcal{T}_h$) of the channel domain Ω via an automatic mesh generator known as ADMESH$^+$ (Conroy et al., 2012). ADMESH$^+$ solves a number of differential equations to calculate a mesh size function that determines
216 local element sizes based on the curvature of the boundary, channel width, and changes in the topography and domain slope to create a high-quality unstructured simplex mesh (the elements are close to equilateral triangles). The only input required by the program is a list of points defining the boundary as well as the topography of the domain.

3.2 A weak form and the semi-discrete equations

Given the finite element partition, $\mathcal{T}_h$, of the domain Ω, we obtain a weak form of equation
221 (20) if we first multiply (20) by a sufficiently smooth test function $\psi(x, y) \in \mathcal{V}$, integrate over each element $\Omega_j \in \mathcal{T}_h$, and then integrate the flux term by parts,

$$\int_{\Omega_j} \frac{\partial U^{(i)}}{\partial t}\,\psi\,dA - \int_{\Omega_j} \mathbf{F}^{(i)}\cdot\nabla\psi\,dA + \int_{\partial\Omega_j} \left(\mathbf{F}^{(i)}\cdot\mathbf{n}\right)\psi\,dS = \int_{\Omega_j} S^{(i)}\,\psi\,dA, \qquad U^{(i)},\ \psi \in \mathcal{V}, \tag{21}$$

for $i = 1,\ 2,\ 3,\ 4$. In the equation above, $\mathbf{n}$ is the outward unit normal to the element boundary $\partial\Omega_j$. Rather than seek solutions to (21) we search for solutions in the finite dimensional subspace of functions defined as

$$\mathcal{V}_{hp} = \left\{\psi : \psi\,|_{\Omega_e} \in \mathcal{P}_p\left(\Omega_j\right), \forall\Omega_j\right\}, \tag{22}$$

226 where $\mathcal{P}_p$ demarcates the space of polynomials of at most degree p that is not necessarily continuous across element boundaries. In other words, given a set of basis functions $\boldsymbol{\phi} = [\phi_0, \phi_1, \ldots, \phi_k]^T$, we express the trial solution ($U_h^{(i)} \in \mathcal{V}_{hp}$) and test function ($\psi_h \in \mathcal{V}_{hp}$) as

$$U_h^{(i)}\Big|_{\Omega_e} = \sum_{l=0}^{k} U_l^{(i)}(t)\phi_l(\mathbf{x}), \tag{23}$$

and

$$\psi_h\Big|_{\Omega_e} = \sum_{l=0}^{k} \psi_l(t)\phi_l(\mathbf{x}), \tag{24}$$

where $\left[U_0^{(i)}, U_1^{(i)}, ..., U_k^{(i)}\right]$ are the time-dependent degrees of freedom of the finite element
231 solution and $i = 1,\ 2,\ 3,\ 4$. We use products of Jacobi polynomials of degree k, $\{\mathcal{P}_p\}_{p=0}^{k}$, as our basis for $\mathcal{V}_{hp}$. The orthogonal triangular basis is defined in terms of a "collapsed coordinate" system that results in a matrix free implementation of the method, see Kubatko

https://doi.org/10.5194/gmd-2020-184
Preprint. Discussion started: 21 September 2020

Geoscientific Model Development Discussions

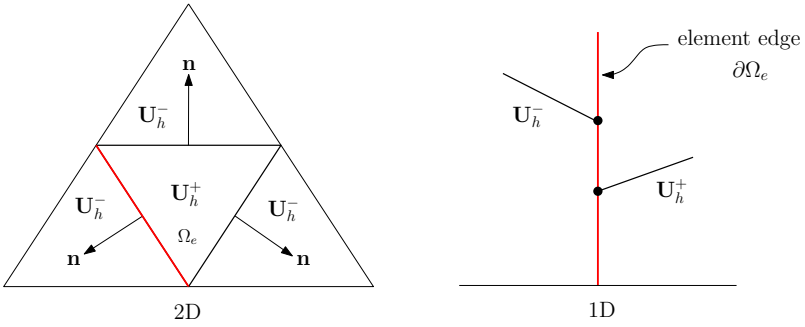

Figure 3: Jump in numerical solution $\mathbf{U}_h$.

et al. (2006) for more details. Substituting $U_h^{(i)}$ and ψ_h into (21) we arrive at the discrete weak form of the problem: find $U_h^{(i)} \in \mathcal{V}_{hp}$ such that for all test functions $\psi_h \in \mathcal{V}_{hp}$, for $i = 1,\ 2,\ 3,\ 4$, the expression,

$$\int_{\Omega_j} \frac{\partial U_h^{(i)}}{\partial t}\,\psi_h\,dA \;-\; \int_{\Omega_j} \mathbf{F}^{(i)}(\mathbf{U}_h)\cdot\nabla\psi_h\,dA \;+\; \int_{\partial\Omega_j}\left(\hat{\mathbf{F}}^{(i)}\cdot\mathbf{n}\right)\psi_h\,dS \;=\; \int_{\Omega_j} S^{(i)}(\mathbf{U}_h)\,\psi_h\,dA, \tag{25}$$

holds over each element $\Omega_j \in \mathcal{T}_h$, where $S^{(i)}(\mathbf{U}_h)$ is the source term evaluated in $\mathcal{V}_{hp}$ and $\hat{\mathbf{F}}^{(i)}$ is a suitably chosen numerical flux.

3.2.1 Numerical flux

The space of functions defined by (22) is not necessarily continuous across element boundaries, and thus, can be dual-valued (see Figure 3 for example). To remedy this inconsistency, we replace the dual-valued flux in (21) with a so-called numerical flux ($\hat{\mathbf{F}}$) that makes use of the left and right limits of the trial solution to produce a single valued flux across a given element's boundary.

More specifically, given an arbitrary function $w_h \in \mathcal{V}_{hp}$ at an element boundary point $\mathbf{x}_i$, we set the left and right limits of the function to $w_h^- \equiv w_h(\mathbf{x}_i^-)$ and $w_h^+ \equiv w_h(\mathbf{x}_i^+)$, respectively. In this work we utilize the local Lax-Friedrichs (LLF) flux, which defines the numerical flux operator as,

$$\widehat{\mathbf{F}}^{(i)}\cdot\mathbf{n} \;=\; \frac{1}{2}\left(\mathbf{F}^{(i,+)}+\mathbf{F}^{(i,-)}\right)\cdot\mathbf{n} \;-\; \frac{1}{2}\,|\lambda_{\max}|\left(U_h^{(i,+)}-U_h^{(i,-)}\right), \quad \text{for } i=1,\ 2,\ 3,\ 4, \tag{26}$$

where $\lambda_{\max}$ is the maximum eigenvalue of the normal (to the element edges) Jacobian matrix. When solutions to (20) are sufficiently smooth, we can rewrite (20) in the quasilinear form,

$$\frac{\partial \mathbf{U}}{\partial t} \;+\; \mathbf{J}_{\mathrm{x}}\,(\mathbf{U})_x \;+\; \mathbf{J}_{\mathrm{y}}\,(\mathbf{U})_y \;=\; \mathbf{S}, \tag{27}$$

https://doi.org/10.5194/gmd-2020-184
Preprint. Discussion started: 21 September 2020

Geoscientific Model Development Discussions

where the Jacobian matrices ($J_{ij} = \frac{\partial F_i}{\partial x_j}$) are,

$$\mathbf{J}_{\mathrm{x}} = \begin{bmatrix} 0 & 1 & 0 & 0 \\ gH - u^2 & 2u & 0 & 0 \\ -uv & v & u & 0 \\ -uT & T & 0 & u \end{bmatrix},$$

and

$$\mathbf{J}_{\mathrm{y}} = \begin{bmatrix} 0 & 0 & 1 & 0 \\ -uv & v & u & 0 \\ gH - v^2 & 0 & 2v & 0 \\ -vT & 0 & T & v \end{bmatrix}.$$

The so-called "normal Jacobian matrix" is then defined by,

$$\mathbf{J}_{\mathrm{n}} = \mathbf{J}_{\mathrm{x}} n_x + \mathbf{J}_{\mathrm{y}} n_y, \tag{28}$$

where n_x and n_y are the $x-$ and $y-$components of the normal edge vector $\mathbf{n}$. In general, if $\mathbf{J}$ is a square $(n \times n)$ matrix with n linear eigenvectors, then it can be decomposed into its eigensystem,

$$\mathbf{J}_x = \mathcal{R}_{(x)} \mathbf{\Lambda}_{(x)} \mathcal{R}^{-1}_{(x)}, \quad \text{and} \quad \mathbf{J}_y = \mathcal{R}_{(y)} \mathbf{\Lambda}_{(y)} \mathcal{R}^{-1}_{(y)}, \tag{29}$$

where $\mathcal{R}_{(\cdot)}$ is the matrix of right eigenvectors, $\mathbf{\Lambda}_{(\cdot)}$ is the diagonal matrix of eigenvalues, and $\mathcal{R}^{-1}_{(\cdot)}$ is the matrix of left eigenvectors (LeVeque et al., 2002). To determine $\Lambda_{(x)}$ and $\Lambda_{(y)}$ we solve for the roots of $\det\left(\mathbf{J}_{(\cdot)} - \lambda \mathcal{I}\right) = 0$, which gives the following eigenvalues,

$$\begin{aligned} \lambda_{1,2} &= u n_x + v n_y, \\ \lambda_3 &= \left(u + \sqrt{gH}\right) n_x + \left(v + \sqrt{gH}\right) n_y, \\ \lambda_4 &= \left(u - \sqrt{gH}\right) n_x + \left(v - \sqrt{gH}\right) n_y. \end{aligned} \tag{30}$$

Each eigenvector ($\mathbf{r}_i^{(\cdot)}$) can be determined by solving $(\mathbf{J}_{(\cdot)} - \lambda_i \mathbf{I})\mathbf{r}_i = \mathbf{0}$ where $\mathbf{I}$ is the identity matrix, $\mathbf{0}$ is a vector of zeros, and $\mathcal{R}_{(\cdot)} = \left[\mathbf{r}_1^{(\cdot)}, \mathbf{r}_2^{(\cdot)}, \mathbf{r}_3^{(\cdot)}, \mathbf{r}_4^{(\cdot)}\right]$. Solving for the eigenvectors we

https://doi.org/10.5194/gmd-2020-184
Preprint. Discussion started: 21 September 2020

Geoscientific Model Development Discussions

have,

$$\mathcal{R}_{(\mathrm{x})} = \begin{bmatrix} 0 & 0 & 1/T & 1/T \\ 0 & 0 & (u+\sqrt{gH})/T & (u-\sqrt{gH})/T \\ 1 & 0 & v/T & v/T \\ 0 & 1 & 1 & 1 \end{bmatrix},$$

and

$$\mathcal{R}_{(\mathrm{y})} = \begin{bmatrix} 0 & 0 & 1/T & 1/T \\ 1 & 0 & u/T & u/T \\ 0 & 0 & (v+\sqrt{gH})/T & (v-\sqrt{gH})/T \\ 0 & 1 & 1 & 1 \end{bmatrix}.$$

We use the full eigensystem in the slope limiting process that stabilizes the method for polynomials of degree greater than or equal to one (Cockburn and Shu, 2001), and we set $\lambda_{\max}$ in the LLF flux to maximum value of $(\lambda_1, \lambda_2, \lambda_3, \lambda_4)$.

3.3 SSP Runge-Kutta time discretizations

Application of the DG spatial operator to (25) results in a system of ODEs for each element,

$$\tilde{\mathbf{M}}_j^{(i)} \frac{d\tilde{\mathbf{U}}_j^{(i)}}{dt} = \mathbf{b}_j^{(i)}, \quad i = 1,\ 2,\ 3,\ 4 \quad \text{and} \quad j = 1, ..., N \tag{31}$$

where N is the number of elements, $\tilde{\mathbf{U}}_j^{(i)} = \left[\, U_{j,0}^{(i)}, U_{j,1}^{(i)}, \ldots, U_{j,k}^{(i)} \,\right]^T$ are vectors of the degrees of freedom, and $\mathbf{b}_j^{(i)} = \left[\, \mathbf{R}_{j,0}^{(i)}, \mathbf{R}_{j,1}^{(i)}, \ldots, \mathbf{R}_{j,k}^{(i)} \,\right]^T$ with,

$$\mathbf{R}_{j,l}^{(i)} = \int_{\Omega_j} \mathbf{F}_j^{(i)} \cdot \nabla \phi_l \; dA \; - \; \int_{\partial\Omega_j} \left(\hat{\mathbf{F}}_j^{(i)} \cdot \mathbf{n} \right) \phi_l \; dS \; + \; \int_{\Omega_j} S_j^{(i)} \; \phi_l \; dA. \tag{32}$$

$\tilde{\mathbf{M}}_j^{(i)}$ is the mass matrix,

$$\tilde{\mathbf{M}}_j^{(i)} = \begin{bmatrix} \int_{\Omega_j} \phi_1\phi_1 \; dA & 0 & \ldots & 0 \\ 0 & \int_{\Omega_j} \phi_2\phi_2 \; dA & 0 & \vdots \\ \vdots & 0 & \ddots & 0 \\ 0 & \ldots & 0 & \int_{\Omega_j} \phi_k\phi_k \; dA \end{bmatrix}.$$

https://doi.org/10.5194/gmd-2020-184
Preprint. Discussion started: 21 September 2020

Geoscientific Model Development Discussions

which is diagonal due to the choice of basis. Left multiplying (31) by the inverse of the mass matrix, we have,

$$\frac{d\tilde{\mathbf{U}}^{(i)}}{dt} = \left(\tilde{\mathbf{M}}_j^{(i)}\right)^{-1} \mathbf{b}_j^{(i)} = \mathcal{L}_{hp}(\tilde{\mathbf{U}}), \quad \text{with} \quad i = 1,\ 2,\ 3,\ 4, \quad \text{and} \quad j = 1, ..., N, \tag{33}$$

where $\mathcal{L}_{hp}$ is the DG spatial operator. We evaluate the integrals in equation (32) using numerical quadrature rules of sufficiently high degree (Kubatko et al., 2006), and discretize (33) with so-called strong-stability-preserving (SSP) Runge–Kutta (RK) methods (Kubatko et al., 2014). The unknown basis coefficients that define the solution over a given element, Ω_j, are advanced in time from t_n to t_{n+1} via,

1. Set $\tilde{\mathbf{U}}_0^{(i)} \leftarrow \tilde{\mathbf{U}}_n^{(i)}$, for $i = 1,\ 2,\ 3,\ 4$.
2. For each stage $r = 1, 2, \ldots, s$, set

$$\tilde{\mathbf{U}}_r^{(i)} \leftarrow \Pi_h \left(\sum_{j=1}^{r} \alpha_{rj} \mathbf{w}^{rj} \right), \quad \mathbf{w}^{rj} = \tilde{\mathbf{U}}_{j-1}^{(i)} + \frac{\beta_{rj}}{\alpha_{rj}} \Delta t\ \mathbf{L}_h \left(\tilde{\mathbf{U}}_{j-1}, t_n + \delta_j \Delta t \right).$$

3. Finally, set $\tilde{\mathbf{U}}_{n+1}^{(i)} \leftarrow \tilde{\mathbf{U}}_s^{(i)}$.

It can be noted that Π_h is a slope limiter that dampens oscillations when polynomial approximations greater than 0 are used for the basis (Cockburn and Shu, 2001), $\delta_j \Delta t$ is a sub-time step of the time step Δt, and the α_{rj} and β_{rj} are coefficients that define the RK method. In particular, α_{rj} and β_{rj} conform to the following constraints,

1. $\alpha_{rj} = 0$ if and only if $\beta_{rj} = 0$,
2. $\alpha_{rj} \geq 0$ and $\beta_{rj} \geq 0$,
3. $\sum_{j=1}^{r} \alpha_{rj} = 1$.

Because we use explicit RK methods the time step of the model is limited by a CFL condition, see Kubatko et al. (2014) for more details.

4 Verification

Verification of the DG solution of the mass and momentum equations in the depth-averaged and full three-dimensional case is well documented and can be found in (Conroy and Kubatko, 2016), (Dawson and Aizinger, 2005) and (Kubatko et al., 2006). To verify our DG solution method for the fully coupled mass, momentum, and energy (depth-averaged) equations we solve a test problem using the method of manufactured solutions. We choose u, v and H so that the depth-averaged mass equation is satisfied exactly. Specifically, we define,

https://doi.org/10.5194/gmd-2020-184
Preprint. Discussion started: 21 September 2020

Geoscientific Model Development Discussions

Table 1: L^2 errors using $\mathcal{P}^0$ for (ζ_h, u_h, v_h, T_h).

Mesh	$\|\|\zeta_h - \zeta\|\|_2$	Order	$\|\|u_h - u\|\|_2$	Order	$\|\|v_h - v\|\|_2$	Order	$\|\|T_h - T\|\|_2$	Order
h_0	3.91	–	8.81	–	9.24	–	2126.3	–
h_1	2.06	0.92	4.48	0.98	4.82	0.94	1227.7	0.79
h_2	1.39	0.97	3.01	0.98	3.30	0.93	875.11	0.84
h_3	0.31	1.08	0.77	0.98	0.77	1.05	218.2	1.00

$$
\begin{aligned}
u &= \hat{u}\exp(-kx), \\
v &= \hat{v}\exp(-kx), \\
H &= h + \hat{\zeta}\exp(\mathrm{i}\,\omega t),
\end{aligned}
\tag{34}
$$

with h = constant, $\hat{u}$ = constant, $\hat{v} = \hat{u}ky$, and $\hat{\zeta} = \exp(-\mathrm{i}\omega\hat{x})$ where $\hat{x} = \exp(kx)/(k\hat{u})$. The dynamical solution consists of a wave propagating in a direction perpendicular to the y-axis with wave number $k = 5.0 \times 10^{-3}$ m^{-1} and frequency $\omega = 2.0 \times 10^{-3}$ s^{-1}. We then set,

$$T = \hat{T}\exp(-k_T x), \tag{35}$$

with $\hat{T} = (y^2 + T_{\text{wall}})$ and substitute (34) and (35) into the math model (1) and evaluate the derivative terms using Matlab's symbolic package. The remainder terms associated with the x-momentum equation and the energy equation are then set as artificial source terms that force the numerical solution to be (34) and (35). The numerical domain consists of a rectangular channel defined by the Cartesian-coordinates $x_0 = 0.0$m, $x_L = 200.0$m, $y_0 = 0.0$m, $y_L = 30.0$m. We assume symmetry about the centerline (at $y = 15$m) and only solve the equations over the half-width of the channel. It can be noted that even though the solutions are guaranteed to remain smooth for all time t (because of the forcing functions) the numerical solution is by no means trivial due to the coupling of the equations through the viscosity. We use four different triangular meshes for our verification. The element size of each mesh is 7.50 m (the so-called h_0 mesh), 3.75 m (h_1), 2.50 m (h_2), and 0.625 m (h_3), respectfully. Results are displayed in Tables 1-3 where it can be noted that the method converges to the analytic solution at rate of approximately $p + 1/2$. Further, using $p = 2$ on the coarsest mesh gives lower errors than $p = 0$ on the finest mesh.

5 Evaluation: Recent eruption of Kilauea Volcano

We evaluate our model using data captured during the 2018 eruption of Kilauea volcano, Hawai'i. The East Rift Zone of Kilauea has erupted repeatedly in historical times, and con-

https://doi.org/10.5194/gmd-2020-184
Preprint. Discussion started: 21 September 2020

Geoscientific Model Development Discussions
Open Access
EGU

Table 2: L^2 errors using $\mathcal{P}^1$ for (ζ_h, u_h, v_h, T_h).

Mesh	$\|\|\zeta_h - \zeta\|\|_2$	Order	$\|\|u_h - u\|\|_2$	Order	$\|\|v_h - v\|\|_2$	Order	$\|\|T_h - T\|\|_2$	Order
h_0	2.30e-2	–	0.33	–	5.82e-2	–	1589.8	–
h_1	4.85e-3	2.25	6.5e-2	2.35	1.50e-2	1.95	367.7	2.11
h_2	1.72e-3	2.56	2.09e-2	2.79	6.33e-3	2.13	154.3	2.14
h_3	1.84e-4	1.63	2.13e-3	1.65	4.32e-4	1.94	6.73	2.26

Table 3: L^2 errors using $\mathcal{P}^2$ for (ζ_h, u_h, v_h, T_h).

Mesh	$\|\|\zeta_h - \zeta\|\|_2$	Order	$\|\|u_h - u\|\|_2$	Order	$\|\|v_h - v\|\|_2$	Order	$\|\|T_h - T\|\|_2$	Order
h_0	1.41e-2	–	6.76e-2	–	6.85e-3	–	17.20	–
h_1	2.56e-3	2.46	2.37e-2	1.51	3.51e-3	0.96	3.04	2.50
h_2	8.00e-4	2.87	8.70e-3	2.47	1.11e-3	2.84	1.09	2.52
h_3	1.24e-4	2.68	1.46e-3	2.57	1.70e-4	2.70	.176	2.63

tinuously since 1983 (Heliker and Mattox, 2003; Wolfe, 1988). A new eruption of unusually large magnitude began May 3, 2018 in the lower part of the East Rift Zone, with fissures opening in the middle of a residential area (Neal et al., 2019). More than 20 fissures opened during the first 12 days of the eruption, erupting slow-moving, unusually high viscosity lava at low effusion rates. The behavior changed on May 18, when much hotter and less viscous lava reached the surface. Advance rates and flow lengths increased, widely impacting property and infrastructure. Complete evacuation orders followed within days. Starting on May 28th, activity focused at Fissure 8, located in the heart of the Leilani Estate subdivision. Fissure 8 remained the source of lava for the remainder of the eruption, until its abrupt stop on August 4th. The lava that erupted from Fissure 8 soon established a channel which flowed north and east of the vent, forming a moderately branched channel network 4 km from the vent. The flow field exhibited transitions between flow types; a clear transition from pahoehoe to ‘a‘a surface texture occurred down slope and is apparent on the thermal map (see Figure 1). Overall, the Fissure 8 lava covered an area of 25 km^2 and supplied at least 1 cubic km of lava (out of at least 1.2 total) over 70 days.

5.1 Observational data

During the 2018 Kilauea eruption, Unoccupied Aerial Systems (UAS) captured a comprehensive time-series of overhead videos of channelized lava (the “Fissure 8” flow). The videography campaign was purposefully designed to collect data for ‘remote rheometry’ by hovering above specific sites spaced 200-1300 m apart along the length of the open channel and revisiting them throughout the duration of the eruption. The proximal (near vent) sites record pahoehoe lava with little crust cover, while the distal sites capture behavior entirely in the ‘a‘a flow regime. Sites within the braided section of the flow recorded video over parallel channels. Over 500 hover videos at the channel sites were acquired over the course of the Fissure 8 eruption between May 30 and August 5. In this paper, we focus on videos

https://doi.org/10.5194/gmd-2020-184
Preprint. Discussion started: 21 September 2020

Geoscientific Model Development Discussions
Open Access
EGU

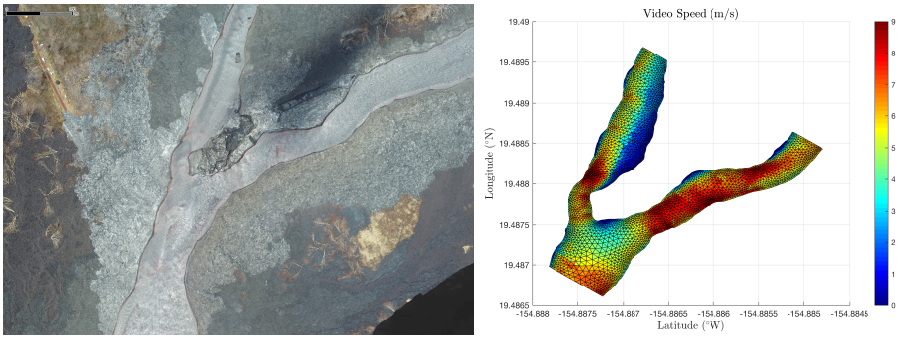

Figure 4: A) Zoomed in view of the section of the braided channel system established by Fissure 8 modeled in this work, near UAS site 8 (See Fig. 1). UAS photo by Ryan Perroy, University of Hawaii-Hilo. B) Map view of the lava surface velocity measured using Optical Flow from videos captured by UAS on June 22nd, 2018. Colors represent magnitude in m/s. Also shown in the discretize finite-element mesh used to evaluate the model.

collected at UAS site 8, capturing a junction point where the main channel split into two branches.

5.1.1 Velocity field measurements

We analyze the UAS hover videos using the Optical Flow technique (Horn and Schunck, 1981; Sun et al., 2010) Optical Flow is a well-known Computer Vision technique used to measure velocities of imaged objects based on the motion of brightness within an image sequence or between frames of a video. Lev et al. (2012) used Optical Flow to measure the two-dimensional surface velocities of laboratory-scale basaltic lava flows. We will follow the same technique as in Lev et al. (2012), tuning parameters to the specifics of the Kilauea 2018 UAS footage. Length scale for video analysis and channel geometry data are provided from camera lens information and the recorded UAS flight altitude and refined using co-registered digital elevation and orthomosaic images produced from additional UAS data collected at the same or very close time.

5.2 Model input

We provide our model with a channel geometry, assumed material properties, inlet velocity, and observed temperature. We use topography data from a pre-eruption digital elevation maps (data from the USGS National Elevation Dataset, with a spatial resolution of 10m/pixel, USGS (2002)) to calculate the gradient of topography (see Figure 5B). We set the inlet velocity equal to values measured from the UAS video analyzed by Optical Flow (Figure 4B). Channel edge geometry is obtained from the velocity field ($V >= 0$) combined with visible identification of channel boundaries in the UAS image. Figure 5 shows the meshed model domain, with colors depicting (a) the elevation and (b) ground slope used to set up the model.

We set the the lava density to $\rho = 1350$ kg/m^3, which, with a nominal gas-free density

https://doi.org/10.5194/gmd-2020-184
Preprint. Discussion started: 21 September 2020

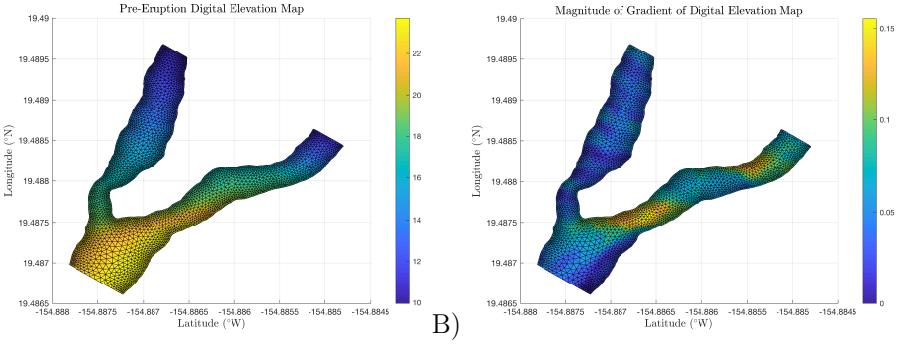

Figure 5: Finite element partition of the modeled section of the braided channel system. Colors corresponds to: (A) topography elevation in meters, and B) ground slope in degrees

of Hawaiian basalts of 2700 kg/m^3 translates to 50% vesicularity. We set the channel inlet temperature to $T = 1152$ C and wall and basal temperatures to $T = 1010$ C and $T = 477$ C, respectively. The rheological constants in relation (4) are set to $A = -4.550$, $B = 5805.30$ and $C = 607.80$. These values were calculated using the calculator by Giordano et al. (2008) and are specific for the composition of the basalt that erupted during June 2018 from Fissure 8 as measured by XRF analysis (Gansecki et al., 2019)). See Table 4 for the coefficient values used in the heat transfer module. It can be noted that because the lava temperature never falls below 950 C in the Kilauea simulations, surface heat loss is solely due to radiation.

5.3 Model results

All model simulations were executed on a Macbook Pro using Intel's Fortran compiler and on average took 56 minutes to execute using a time step dt = 0.05 secs. The model's initial conditions were set to the solution of a linearized form of (1) with $\zeta = 0$ and $h = 10$ m. Inlet conditions are steady in time and we set $\boldsymbol{\tau}_{\text{yield}} = 0$ in the Herchel-Bulkley model.

Figure 6 shows the lava velocities calculated for the entire domain by our model using exponent values in the viscosity model (3) of $n = 1$ (Newtonian) and $n = 2$ (shear-thickening). Key features of the observed flow field, such as the increase in speed after the constriction in the northern branch and the stagnation at the channel split point, are present in both Figures. The overall magnitude of the velocity – up to 9 m/s – is also in agreement with the observations.

5.4 Discussion

We evaluate the quality of the fit between the model and the observations by comparing the modelled speed with the observed speed for different power-law exponent (n) values, shown in Figure 7. Two areas of relatively large error are clear in the southern branch. We attribute these mostly to uncertainties in the underlying topography data. We use a coarse pre-eruption DEM for an area where the overall slopes are very gradual (2-3 degrees). The mesh and model resolution is very high compared to the coarseness of the DEM (only 10

https://doi.org/10.5194/gmd-2020-184
Preprint. Discussion started: 21 September 2020

Geoscientific Model Development Discussions

Table 4: Value of thermal coefficients.

Coefficient	Meaning	Value used in Kilauea simulation
ϵ	Emissivity	0.85
σ_b	Stefan-Boltzmann constant	5.670×10^{-8} J$\cdot$ m$^{-2}\cdot$ s$^{-1}\cdot$ K^{-4}
c_p	Heat capacity	837 J $\cdot$ kg$^{-1}\cdot$ K^{-1}
k_c	heat transfer coefficient	200.0 W$\cdot$m$^{-1}\cdot$ K^{-1}
k_T	thermal conductivity of the ground	0.90 W$\cdot$m$^{-1}\cdot$ K^{-1}
$\tilde{k}_T$	thermal conductivity of the thermal boundary layer	0.10 W$\cdot$m$^{-1}\cdot$ K^{-1}

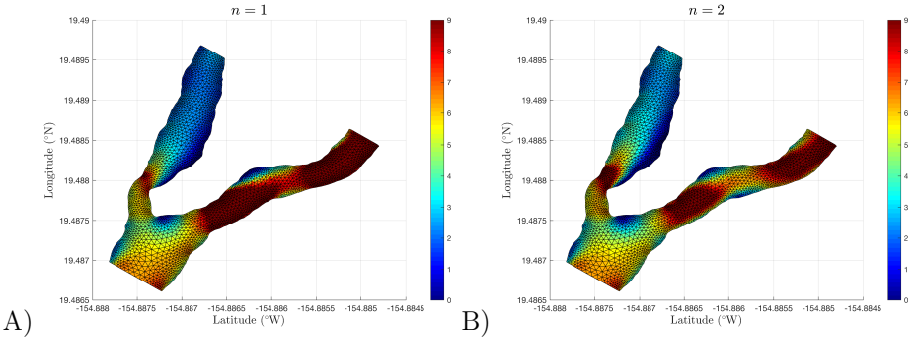

A) B)

Figure 6: Map view of modeled speed using a value of (A) $n = 1$ and (B) $n = 2$ in the viscosity model. Colors represent velocity magnitude in m/s.

https://doi.org/10.5194/gmd-2020-184
Preprint. Discussion started: 21 September 2020


Geoscientific Model Development Discussions

DEM grid points across the model), which can lead to inaccuracies in slope estimates. In addition, the DEM is from before the eruption, while the velocity data was captured a few weeks after the channel was established. It is possible that by that time, some lava already deposited on the bottom of the channel and modified the topography.

An additional source of misfit could be due to the bottom stress calculation. We calculate the thickness of the virtual layer over which the velocity transitions from the depth-integrated velocity to a value of zero (at the bottom boundary) via a two-layer model of vorticity. The two layers correspond to a mixed upper layer and a non-mixed bottom layer where the lava is loosing heat due to conduction. While this approach seems to be valid in terms or reproducing lava flow thicknesses observed by USGS surveys (USGS Hawaii Volcano Observatory, 2019) which place lava thicknesses between 5 m - 15 m, (alternative methods produce flows that are 3 times too thick), the two-layer model still is a simplification of reality that most likely introduces some errors.

Further, because we are limited to surface speed observations our error metrics will unavoidably have a misfit in them due to the fact that modeled speeds are depth-averaged. This effect will be small in regions of the channel where the Reynolds number is high because the lava speed will be more uniform over its thickness. However, in areas where the Reynolds number is low(er), model speeds will be less than observations. This is because the section of channel we modeled has minimal crust cover, and therefore, there is relatively zero stress at the top boundary of the lava flow meaning that lava speed should reach a maximum at the surface. This effect is evident in the northern portion of the northern channel and the portion of the southern channel between Latitude -154.886 °W and -154.8855 °W.

An interesting aspect of the model worth drawing attention to is how a change in the value of n in the viscosity model affects numerical results. Figures 7 and 8 reveal that the overall fit improves with increasing n values which corresponds to shear-thickening in our model. Similarly, the thicknesses predicted by our model for larger power-law exponent values (Figure 9) are closer to the range of thicknesses (5-15 m) measured by USGS survey (USGS Hawaii Volcano Observatory, 2019) and the apparent viscosity calculated by our model (shown in Figure 10) for large n values is similar to rough estimates by the USGS (W. Thelen, pers. comm., 2018).

The lower error measures produced by our model for shear-thickening behaviour is a departure from other studies that find lava to behave as a shear-thinning fluid when crystals and/or bubbles are present (e.g., Castruccio et al., 2010; Costa et al., 2009; Pinkerton, 1995). The disparity can most likely be attributed to differences in the crystal/bubble content of the lava. In the studies of Castruccio et al. (2010), Costa et al. (2009), and Pinkerton (1995) the crystal/bubble content of the lava studied was low ($< 20\%$). Samples taken from the Fissure 8 flow during and after the eruption show a wide range of crystallinity and vesicularity, often with very high vesicle fraction of over 50% (Halverson et al., 2020). The improved overall fit of our model for higher n values is most likely due to this high vesicle fraction and is consistent with the lab experiments of Smith (1997) and Lev et al. (2020) that show high bubble/crystal content can produce shear-thickening behavior. In fact, in the experiments of Sayag and Worster (2013), shear thickening behavior for a constant volume of fluid (as in our investigation) produce flow thicknesses that are less than the shear-thinning case, which is visible in our results in Figure 9. We conjecture that the increase in the viscosity is due to the fact that as the strain rate increases, the bubbles re-arrange in a fashion that makes

https://doi.org/10.5194/gmd-2020-184
Preprint. Discussion started: 21 September 2020

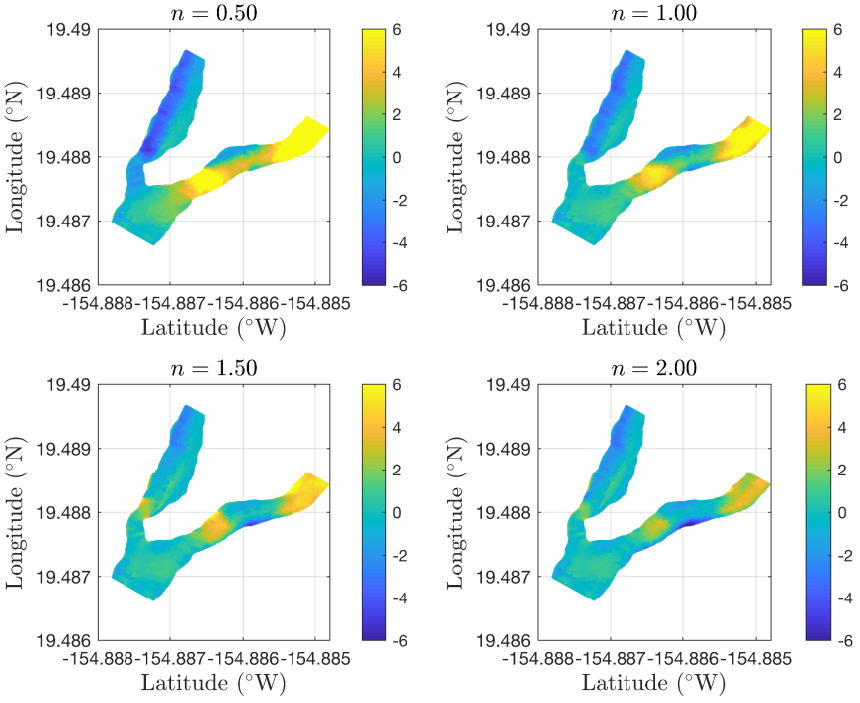

Figure 7: Map view of the difference between modeled lava speed and surface speed obtained from UAS video capture for various power law exponents. Colors represent difference in meters per second.

it harder for the lava to flow. This effect should be especially pronounced in areas where the
426 strain rate is high (think of the stress associated with solid boundaries in turbulence and how the vorticity created at these boundaries could cause bubbles to run into each other, impeding the flow). This effect is apparent in Figure 10 for the case $n = 2$, where the effective viscosity is low except in regions of high strain and high(er) Reynolds number, such as near the constriction in the northern channel, at the channel walls where the slope is high in the
431 southern channel, and at the bend area in the southern channel. In the future we will explore mathematical relationships that allow n to be a function of the bubble/crystal content of the lava as well as examine the sensitivity of the model to non-Newtonian rheological parameters. We plan to infer the best fitting values for these parameters for a range of locations and times for the Fissure 8 lava flow.

https://doi.org/10.5194/gmd-2020-184
Preprint. Discussion started: 21 September 2020

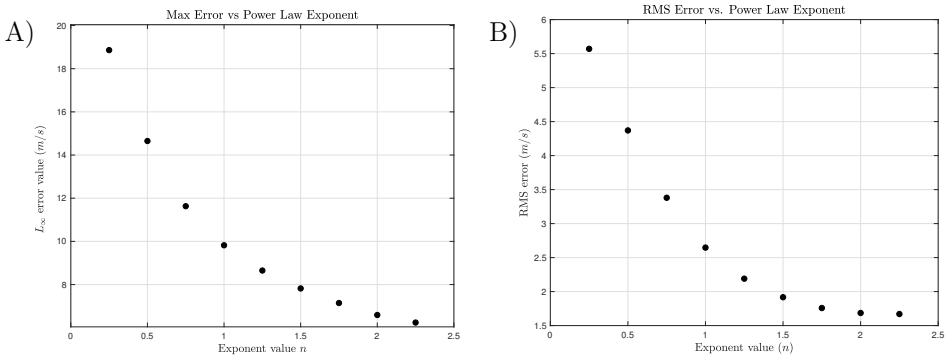

Figure 8: A) Maximum error in model speed versus power law exponent. B) Root mean square error in model speed versus power law exponent.

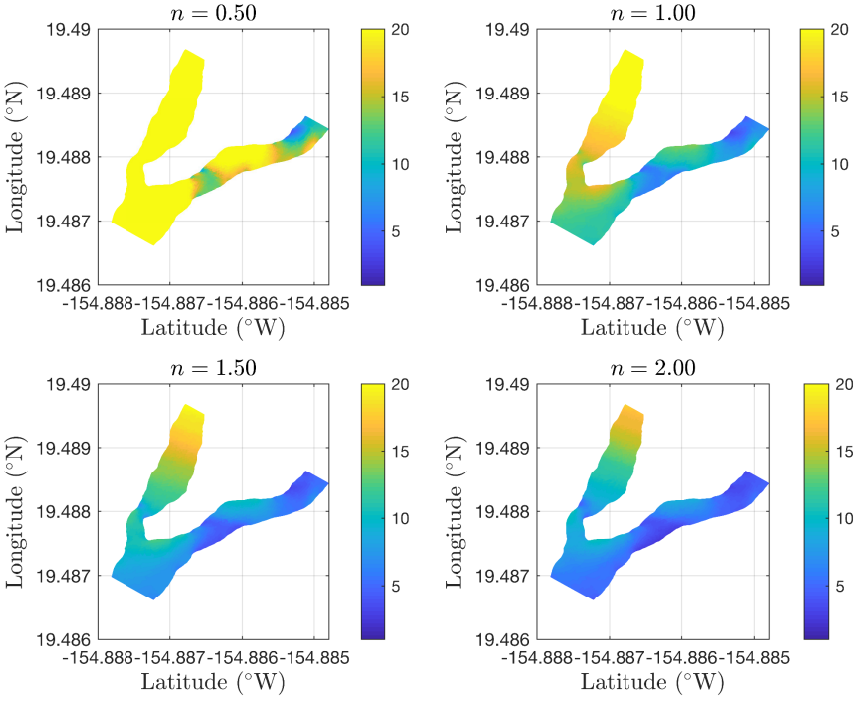

Figure 9: Map view of the modeled lava thickness for various power law exponents. Colors represent lava thickness in meters. Notice that the lava becomes thinner as the value of n increases.

https://doi.org/10.5194/gmd-2020-184
Preprint. Discussion started: 21 September 2020

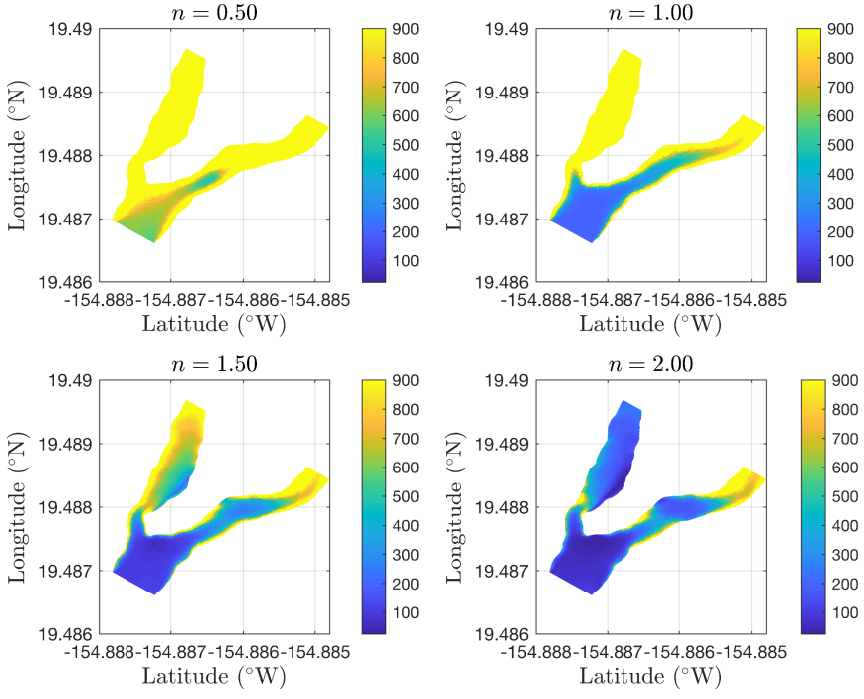

Figure 10: Map view of the effective modeled lava viscosity for various power law exponents. Colors represent viscosity in Pascal seconds.

https://doi.org/10.5194/gmd-2020-184
Preprint. Discussion started: 21 September 2020

Geoscientific Model Development Discussions

6 Conclusions

We present a novel numerical model for quantifying high-speed lava flows in complex channels. The math model consists of depth-averaged equations of mass, momentum, and energy and the equations are closed via a non-linear viscosity model. Because we use discontinuous Galerkin methods to discretize the math model we are able to capture non-smooth transitions that can occur in lava flows, e.g. jumps in temperature, shear, and viscosity, see Figure 10. We overcome a major limitation to many depth-integrated models in terms of the need to use an adjustable friction coefficient by solving a heat transfer boundary layer problem and by calculating the thickness of a virtual layer over which the velocity transitions from the depth-integrated velocity to a value of zero (at the bottom boundary) via a two-layer model of vorticity. This novel approach results in lava flow thicknesses that are in the range of observed values as compared to simple linear schemes that produce flow thicknesses that are 3 times too thick. Further, our use of unstructured triangular meshes allows the model to accurately resolve complex braided channel systems that are commonly produced by basaltic lava flows. This was demonstrated on a section of the complex braided channel system that was created by the Fissure 8 flow from the 2018 Kilauea Lower East Rift Zone eruption with model results matching observational results quantitatively well. Future work will include using our new versatile model as a tool to infer lava properties and flux during volcanic crises.

Computer code and data

The computer code and data used in this investigation can be found at `https://zenodo.org/badge/latestdoi/267726380`.

Author contribution

CJC developed the model code and performed all model simulations. EL assisted in the Unoccupied Aerial System (UAS) data collection and utilized the Optical Flow technique to quantify lava velocities from the UAS data. CJC prepared the manuscript with contributions from EL.

Competing interests

The authors declare that they have no conflict of interest.

Financial support

This investigation was supported by the National Science Foundation under Grant No. EAR-1654588.

https://doi.org/10.5194/gmd-2020-184
Preprint. Discussion started: 21 September 2020

Geoscientific Model Development Discussions

References

Baloga, S., Spudis, P. D., and Guest, J. E. The dynamics of rapidly emplaced terrestrial lava flows and implications for planetary volcanism. *Journal of Geophysical Research: Solid Earth*, 100(B12):24509–24519, 1995.

Castruccio, A., Rust, A. C., and Sparks, R. S. J. Rheology and flow of crystal-bearing lavas: Insights from analogue gravity currents. *Earth and Planetary Science Letters*, 297: 471–480, 2010. doi: 10.1016/j.epsl.2010.06.051.

Castruccio, A., Rust, A. C., and Sparks, R. S. J. Assessing lava flow evolution from post-eruption field data using Herschel-Bulkley rheology. *Journal of Volcanology and Geothermal Research*, 275:71–84, 2014. doi: 10.1016/j.jvolgeores.2014.02.004.

Cockburn, B. and Shu, C.-W. Runge–kutta discontinuous galerkin methods for convection-dominated problems. *Journal of scientific computing*, 16(3):173–261, 2001.

Connor, L. J., Connor, C. B., Meliksetian, K., and Savov, I. Probabilistic approach to modeling lava flow inundation: a lava flow hazard assessment for a nuclear facility in armenia. *Journal of Applied Volcanology*, 1(1):1–19, 2012.

Conroy, C. J. and Kubatko, E. J. hp discontinuous galerkin methods for the vertical extent of the water column in coastal settings part i: Barotropic forcing. *Journal of Computational Physics*, 305:1147–1171, 2016.

Conroy, C. J., Kubatko, E. J., and West, D. W. Admesh: An advanced, automatic unstructured mesh generator for shallow water models. *Ocean Dynamics*, 62(10-12):1503–1517, 2012.

Costa, A., Caricchi, L., and Bagdassarov, N. A model for the rheology of particle-bearing suspensions and partially molten rocks. *Geochemistry, Geophysics, Geosystems*, 10(3), 2009.

Crisci, G. M., Rongo, R., Di Gregorio, S., and Spataro, W. The simulation model SCIARA: the 1991 and 2001 lava flows at Mount Etna. *J. Volcanol. Geotherm. Res.*, 132:253–267, 2004-04. doi: 10.1016/S0377-0273(03)00349-4.

Dawson, C. and Aizinger, V. A discontinuous galerkin method for three-dimensional shallow water equations. *Journal of Scientific Computing*, 22(1-3):245–267, 2005.

Dawson, C., Kubatko, E. J., Westerink, J. J., Trahan, C., Mirabito, C., Michoski, C., and Panda, N. Discontinuous galerkin methods for modeling hurricane storm surge. *Advances in Water Resources*, 34(9):1165–1176, 2011.

Dietterich, H. R. and Cashman, K. V. Channel networks within lava flows: Formation, evolution, and implications for flow behavior. *Journal of Geophysical Research (Earth Surface)*, 119:1704–1724, 2014-08. doi: 10.1002/2014JF003103.

https://doi.org/10.5194/gmd-2020-184
Preprint. Discussion started: 21 September 2020

Geoscientific Model Development Discussions

Gansecki, C., Lee, R. L., Shea, T., Lundblad, S. P., Hon, K., and Parcheta, C. The tangled tale of Kīlaueas 2018 eruption as told by geochemical monitoring. *Science*, 366(6470), 2019.

Giordano, D., Russell, J., and Dingwell, D. Viscosity of magmatic liquids: A model. *Earth and Planetary Science Letters*, 271:123–134, 2008. ISSN 0012-821X.

Griffiths, R. W. The dynamics of lava flows. *Annual Review of Fluid Mechanics*, 32(1): 477–518, 2000.

Halverson, B., Whittington, A., Hammer, J., deGraffenried, R., Lev, E., Dietterich, H., Patrick, M., Parcheta, C., Carr, B., Zoeller, M., Trusdell, F., and Llewellin, E. Vesicularity and rheology of the kilauea 2018 lava flows. Goldschmidt conference, 2020.

Harris, A. J. and Rowland, S. K. Flowgo 2012: An upyeard framework for thermorheological simulations of channel-contained lava. *Hawaiian Volcanoes: From Source to Surface*, 208: 457, 2015.

Heliker, C. and Mattox, T. N. The first two decades of the pu u o'ö-küpaianaha. *US Geological Survey Professional Paper*, 1676(1676):1, 2003.

Herschel, W. H. and Bulkley, R. Konsistenzmessungen von gummi-benzollösungen. *Colloid & Polymer Science*, 39(4):291–300, 1926.

Horn, B. K. and Schunck, B. G. Determining optical flow. *Artificial intelligence*, 17(1-3): 185–203, 1981.

Kelfoun, K. and Vargas, S. V. Volcflow capabilities and potential development for the simulation of lava flows. *Geological Society, London, Special Publications*, 426:SP426–8, 2015.

Kubatko, E. J., Westerink, J. J., and Dawson, C. hp discontinuous galerkin methods for advection dominated problems in shallow water flow. *Computer Methods in Applied Mechanics and Engineering*, 196(1-3):437–451, 2006.

Kubatko, E. J., Yeager, B. A., and Ketcheson, D. I. Optimal strong-stability-preserving runge–kutta time discretizations for discontinuous galerkin methods. *Journal of Scientific Computing*, 60(2):313–344, 2014.

Lev, E., Spiegelman, M., Wysocki, R. J., and Karson, J. A. Investigating lava flow rheology using video analysis and numerical flow models. *Journal of Volcanology and Geothermal Research*, 247:62–73, 2012.

Lev, E., Birnbaum, J., Conroy, C. J., Whittington, A., Halverson, B., Hammer, J., and Llewellin, E. The rheology of three-phase lavas and magmas. Goldschmidt conference, 2020.

LeVeque, R. J. et al. *Finite volume methods for hyperbolic problems*, volume 31. Cambridge university press, 2002.

https://doi.org/10.5194/gmd-2020-184
Preprint. Discussion started: 21 September 2020

Geoscientific Model Development Discussions

Neal, C., Brantley, S., Antolik, L., Babb, J., Burgess, M., Calles, K., Cappos, M., Chang, J., Conway, S., Desmither, L., et al. The 2018 rift eruption and summit collapse of kīlauea volcano. *Science*, 363(6425):367–374, 2019.

Patrick, M., Dehn, J., and Dean, K. Numerical modeling of lava flow cooling applied to the 1997 okmok eruption: Approach and analysis. *Journal of Geophysical Research: Solid Earth*, 109(B3), 2004.

Patrick, M. R., Dietterich, H. R., Lyons, J. J., Diefenbach, A. K., Parcheta, C., Anderson, K. R., Namiki, A., Sumita, I., Shiro, B., and Kauahikaua, J. P. Cyclic lava effusion during the 2018 eruption of kilauea volcano. *Science*, 366(6470), 2019. ISSN 0036-8075. doi: 10.1126/science.aay9070. URL `https://science.sciencemag.org/content/366/6470/eaay9070`.

Pinkerton, H. Rheological properties of basaltic lavas at sub-liquidus temperatures: laboratory and field measurements on lavas from Mount Etna. *J. Volcanol. Geotherm. Res.*, 68: 307–323, 1995. doi: 10.1016/0377-0273(95)00018-7.

Sayag, R. and Worster, M. G. Axisymmetric gravity currents of power-law fluids over a rigid horizontal surface. *Fluid Mechanics*, 716:R5–1–R5–12, 2013.

Schlichting, H., Gersten, K., Krause, E., Oertel, H., and Mayes, K. *Boundary-layer theory*, volume 7. Springer, 1968.

Smith, J. V. Shear thickening dilatancy in crystal-rich flows. *Volcanology and Geothermal Research*, 79:1–8, 1997.

Sun, D., Roth, S., and Black, M. J. Secrets of optical flow estimation and their principles. In *2010 IEEE computer society conference on computer vision and pattern recognition*, pages 2432–2439. IEEE, 2010.

USGS. National elevation dataset, 2002.

USGS Hawaii Volcano Observatory. Kilauea 2018 lower east rift zone lava flow thicknesses: a preliminary map, 2019. URL `https://www.usgs.gov/maps/k-lauea-2018-lower-east-rift-zone-lava-flow-thicknesses-a-preliminary-map`.

Vicari, A., Alexis, H., Del Negro, C., Coltelli, M., Marsella, M., and Proietti, C. Modeling of the 2001 lava flow at Etna volcano by a Cellular Automata approach. *Environmental Modelling & Software*, 22(10):1465–1471, 2007. ISSN 1364-8152.

Wolfe, E. W. The puu oo eruption of kilauea volcano, hawaii: Episode 1 through 20, january 3, 1983, through june 8, 1984. *US Geol. Serv. Prof. Paper*, 1463:251p, 1988.